Materials Views

www.MaterialsViews.com

ADVANCED
ENERGY
MATERIALS

www.advenergymat.de

FULL PAPER

Li4Ti5O12 Nanocrystals Synthesized by Carbon Templating from Solution Precursors Yield High Performance Thin Film Li-Ion Battery Electrodes

*Xiaoguang Hao and Bart M. Bartlett**

Nanocrystals of Li4Ti5O12 (LTO) have been prepared by processing an ethanol-toluene solution of LiOEt and Ti(OiPr)4 using a carbon black template. The mechanism of crystal growth has been tracked by SEM and TEM microscopies. The resulting nanocrystals grown using the carbon template (C-LTO) show less aggregation than materials prepared from solution without the template (S-LTO), which is reflected in higher surface area (27 m2/g) and concomitantly smaller particle size (58 nm) for C-LTO compared to 20 m2/g and 201 nm for S-LTO. Electrochemically, thin-film electrodes composed of C-LTO demonstrate reversible cycling, storing ~160 mAh/g at both 1 C (175 mA/g) and 10 C current. Important is that resistance to charge transfer between the C-LTO nanocrystals and added conducting carbon is 3 times smaller than that for S-LTO. Accordingly, C-LTO shows excellent rate capability, maintaining an energy-storage capacity >150 mAh/g even at 100 C current. These characteristics solidify C-LTO a suitable replacement for carbon as a Li-ion battery anode.

1. Introduction

There is growing interest in alternatives to graphite as the anode material for lithium-ion batteries that improve safety without sacrificing performance. Specifically, the challenge is to find a thermodynamically stable material in which no solid-electrolyte interface (SEI) layer grows.[1,2] The formation and growth of the SEI layer in graphite-containing batteries are well-documented, but remain poorly understood. Meanwhile, recent work has focused on nanomaterials composed of other group 14 elements such as silicon[3] and germanium[4] which show significantly higher energy density than carbonaceous anodes. However, these materials have the drawback of large volume changes upon lithium insertion, which leads to electrode pulverization on repeated cycling with rapid capacity fade. Pure oxide-based intercalation materials such as Li4Ti5O12 (LTO) have the advantage that volume changes in the host lattice are negligible upon lithium insertion.[5–7] On the other hand, the low-voltage limit (commonly set at 1.0 V *vs.* Li+/0) of oxides is higher, resulting

in a decrease in energy density. Despite this drawback, LTO remains a promising anode material for Li-ion batteries because of its stability.

To date, no anode material is flawless, and the fundamental limitations to using LTO prepared by existing methods are that the rate of lithium-ion diffusion is too slow (10^{-14} to 10^{-17} cm2/s)[8] and the compound suffers from poor electrical conductivity (<10^{-13} S/cm).[9] The former problem requires the use of nanoparticles to shorten the path of lithium diffusion in the solid state.[10–12] The latter problem is typically addressed by adding electrically conductive carbon when preparing an electrode slurry,[13–17] but requires low resistance to charge transfer between the LTO nanoparticles and added carbon.

The need to solve both problems simultaneously generates a scientific dilemma. There are many synthesis routes described that result in nanoparticles, including hydrothermal synthesis[18–21] or using a soft template in sol-gel processing methods.[22–24] However, the growing nanoparticles tend to aggregate due to their high surface energies, and as a result, the electrode is composed of micron-sized aggregates. The problem with aggregates is that too many LTO surfaces are in contact with other LTO crystallites, and therefore not available to contact the conducting carbon. Electrodes fabricated from these agglomerates are subject to large polarization losses. Three dimensionally ordered microporous (3DOM) Li4Ti5O12 and nanoscale porous framework electrode have also been introduced.[25,26] However, high rate capability is not achievable due to the lack of electrical contact with conductive carbon in those electrodes.

To resolve this predicament, we describe in this manuscript for the first time the synthesis of LTO nanocrystals from solution-phase precursors using a carbon-templated growth process. In this process, crystal growth is complete (all of the nutrients are consumed) and the surfaces are annealed at high temperature at nearly the same rate at which the template burns off. Therefore, the LTO product is composed of regularly shaped octahedra whose crystal facets point along the [011] direction. Advantageously, this direction is the one from which lithium ions insert from the electrolyte, and the electrochemical characteristics far exceed those of typical nanoparticles grown without such a template. When 30 μm thin-film electrodes composed

X. Hao, Prof. B. M. Bartlett
Department of Chemistry
University of Michigan
930 N. University Ave. Ann Arbor, MI 48109-1055 USA
E-mail: bartmb@umich.edu

of LTO nanocrystals are cycled against Li-foil, the cells show highly reversible electrical energy storage of over 250 Wh/kg at the slow rate of 1 C (the current required to charge/discharge the battery in one hour, 175 mA/g). Remarkably, the energy density remains large as the power increases: 190 kW/kg, at 100 C (charge/discharge in 36 s).

2. Results

2.1. Synthesis and Characterization of LTO Nanocrystals

In the present study, a solution-based method starting from alkoxide precursors of lithium and titanium was applied in order to obtain atomic-level mixing from which to synthesize $Li_4Ti_5O_{12}$ (LTO). The synthon lithium ethoxide is the first prepared on a Schlenk line by reacting metallic lithium with absolute ethanol, liberating hydrogen in the process. The other synthon, titanium isopropoxide is prepared as a 0.48 M solution in toluene, and the two reactants are mixed – 4 parts LiOEt to 5 parts $Ti(O^iPr)_4$. We then add additional toluene such that the precursor mixture is 2:3 EtOH:PhMe; this combination slows solvolysis. ^{1}H-NMR spectroscopy (Figure S1) shows that the as-synthesized precursor is composed of isopropoxide and ethoxide, and the solution is stable for several days under ambient room conditions, noted by the unchanged spectrum after storage.

Isolated LTO nanocrystals form from a templated synthesis using this precursor solution and carbon (acetylene) black. In a typical synthesis, we add 1 g of carbon black per 50 mL of precursor solution prior to removing the solvents. Carbon black is a form of amorphous carbon whose role is to prevent aggregation of the growing nanocrystals during annealing. In order to achieve the minimum carbon loading and to minimize interparticle contact, we centrifuged the samples to eliminate as much excess solvent as possible prior to annealing. The annealing scheme was determined from the results of thermogravimetric analysis (Figure S2). Solvent evaporation continues as the temperature is ramped to ~200 °C, irrespective of the presence of carbon black. The two syntheses are distinguished above 500 °C, where an abrupt change in mass occurs for the material containing carbon black. This mass change corresponds to the ignition of carbon black; the sample glows bright

red, commensurate with burning carbon. No further mass loss is observed above 600 °C. Above this temperature, there is no carbon remaining, further supported by Raman spectroscopy (Figure S3).[25]

Figure 1a shows SEM and HR-TEM images of the resulting nanocrystals from the carbon-templated synthesis (C-LTO). The material is composed of 67 ± 17 nm crystallites with distinct octahedral facets, with a histogram of the particle size distribution shown in Figure S4. Images of the carbon template in Figure 1b show that it too is composed of ~70 nm particles, thus dictating the particle size of the product. Most important, the particles resulting from annealing the precursor solution (S-LTO) without adding the carbon template are illustrated in Figure 1c. Here, we observe micron-sized aggregates.

The powder X-ray diffraction pattern in **Figure 2** confirms that the crystalline products obtained are spinel, regardless of the presence or absence of the template. Rietveld analysis of the diffraction patterns (Figures S5 and S6 with associated Tables S1–S4) give nearly identical lattice parameters, 8.362 and 8.363 Å for C-LTO and S-LTO respectively, in agreement with what has been reported.[27] The only notable difference is in the intensities of the reflections of the two samples, which is due to the smaller particles resulting from the C-LTO preparation; defining the crystalline domain size by the Scherrer equation[28] in our Rietveld refinement corroborates our SEM findings: 58 nm suggests nearly single crystals of C-LTO; the domain size of S-LTO is much larger, 201 nm. The selected area electron diffraction pattern (Figure S7) of the individual C-LTO nanocrystal in the inset of Figure 1a shows exposed facets that point along [011], the direction along which Li-ion channels are organized, also illustrated in Figure S7. This result is similar to what we recently report for $LiNi_{0.5}Mn_{1.5}O_4$ spinel materials synthesized by low temperature hydrothermal methods.[29]

Finally, the surface area of C-LTO is slightly larger, 27 m^2/g, compared to 20 m^2/g for S-LTO as determined by BET analysis of N_2 sorption isotherms (Figure S8). The high surface area of these LTO samples will result in high rate capability (i.e.—high power) electrodes. However, the negligible aggregation in C-LTO nanocrystals helps to retain a large energy density as well. The lack of aggregation is demonstrated in the section 2.3 of the results.
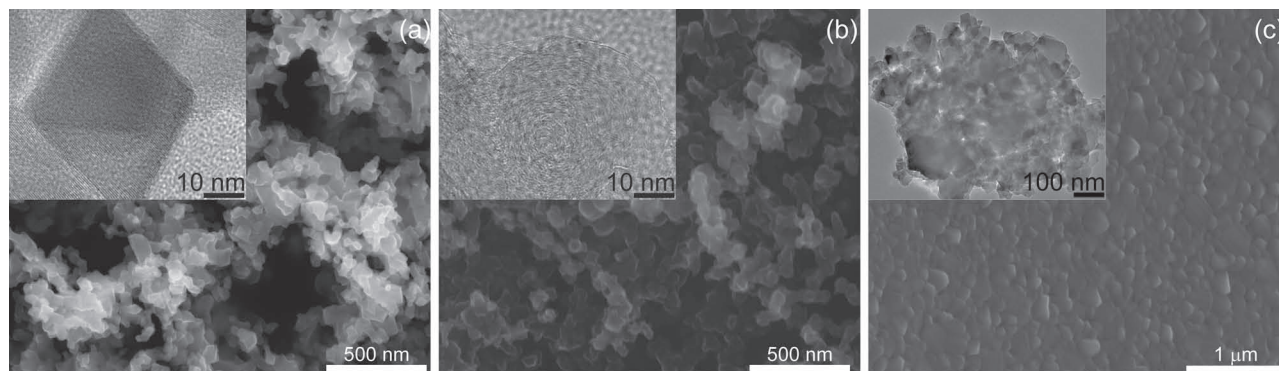

Figure 1. (a) SEM and HR-TEM images of C-LTO nanocrystals; (b) the carbon template; (c) and the S-LTO aggregates.
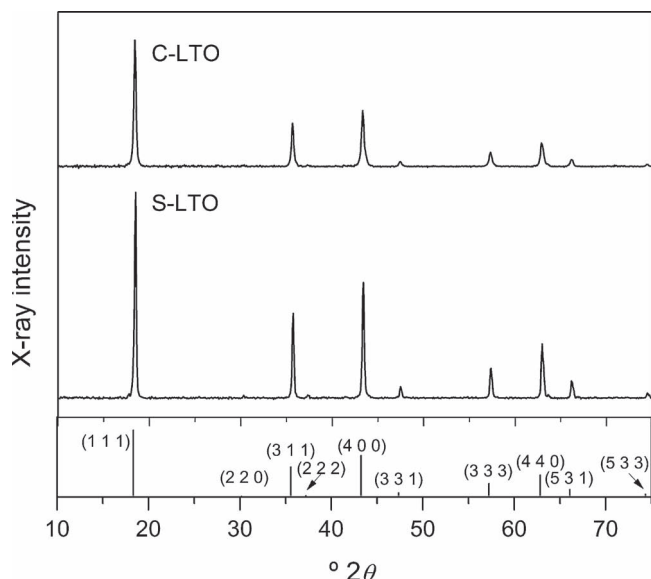
www.MaterialsViews.com

ADVANCED
ENERGY
MATERIALS
www.advenergymat.de

FULL PAPER

Figure 2. (a) XRD patterns for C-LTO (top) and S-LTO (bottom). The indexed pattern for LTO is presented in gray underneath.

2.2. Details of the Crystal Growth Mechanism

In order to elucidate the crystal growth mechanism, we performed temperature-dependent studies of the C-LTO synthesis, returning to our TGA trace (Figure S2). There are two plateaus of stability—one between 200 and 500 °C, and the second above 600 °C. TEM images shown in **Figure 3** give the account of nanocrystal growth. First, in Figure 3a, we observe only the carbon template at room temperature; it is composed of 50 nm spheres, as was highlighted above. Figure 3b shows the image of the precursor solution loaded with the carbon template. Not surprisingly, there is no order since this material has not yet been annealed. During the synthesis, carbon is completely soaked with the precursor solution, and lithium and titanium are evenly dispersed on the surface as evidenced by the energy dispersive X-ray spectra and map in Figure S9.

After annealing the sample to 450 °C (within the first plateau of stability) for 1 h, order emerges. Figure 3c shows crystalline domains that are ~10 nm in diameter growing off of the carbon black template. Curiously, the image in Figure 3d is also

captured after annealing at 450 °C for 1 h. Here, much larger crystalline domains are observed with residual carbon attached, which suggests that particle growth is concomitant with template removal (carbon is oxidized to carbon dioxide). Figure 3e shows the final product to be regular octahedra after annealing to 700 °C. By controlling the annealing temperature and time, we conclude that crystal size is ultimately limited by the size of the template. And, since crystal growth consumes nutrients localized on the carbon black template surface, minimal aggregation results.

2.3. Electrochemistry

$Li_4Ti_5O_{12}$ can uptake three lithium ions during the charging process, corresponding to a theoretical energy storage capacity of 175 mAh/g.[30,31] **Figure 4**a shows the gravimetric capacity of thin-film electrodes composed of either C-LTO or S-LTO materials cycled at 1 C current. In the C-rate convention, n C current represents the load required to charge/discharge the theoretical capacity in $1/n$ hours. For an electrode composed of 1 mg LTO, 1 C corresponds to a current density of 175 μA/cm^2. Lithium insertion and extraction occur as a two-phase mixture of $Li_4Ti_5O_{12}$ and $Li_7Ti_5O_{12}$, leading to a flat, constant voltage plateau (a consequence of the Gibbs's phase rule) at 1.55 V vs. Li$^{+/0}$.[32] However, slow Li$^+$ diffusion and charge transfer tend to lower the capacity and also cause hysteresis between the charge and discharge profiles. Both materials show similarly excellent capacity retention for the first 100 cycles, with an intial capacity of 167 mAh/g (at cycle 4) and 160 mAh/g (97.6% retention) at the end of the test. The initial charge capacity of the material nearly reaches the theoretical capacity value. Voltage curves for the 50th charge and discharge cycles are higlighted in Figure 4b. Regardless of the preparation method, LTO shows a polarization voltage gap (hysteresis) of 65 mV; the charging plateau potentials were 1.53 V in both cases. This observation suggests that neither charge transfer nor Li$^+$ diffusion within LTO are limited by the difference in particle size or by aggregation at low current.

Next, C-LTO and S-LTO materials were cycled at a rate of 10 C (1.75 mA/cm^2), shown in Figure 4c. Both electrodes still show excellent capacity retention after 100 cycles at 10 C: 97.6% for C-LTO and 94.1% for S-LTO. However, two key differences arise as we plot the voltage curve for the 50th cycle
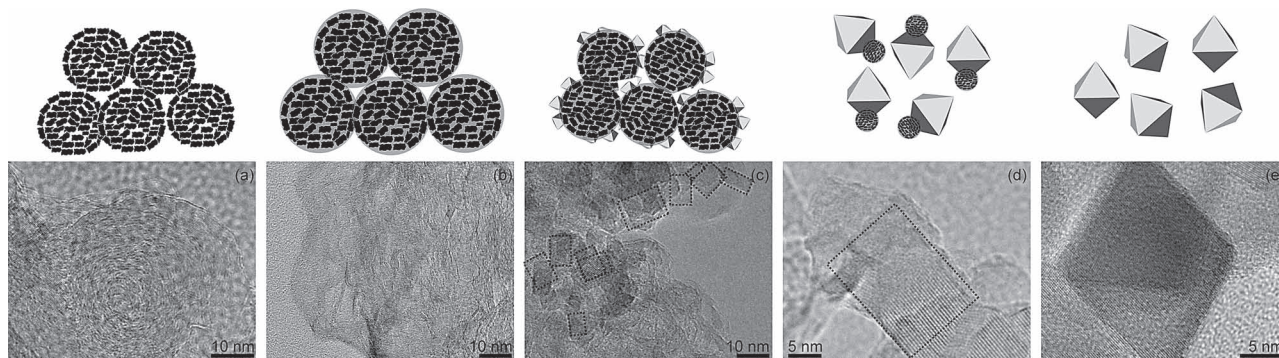

Figure 3. TEM images highlighting the growth mechanism of C-LTO nanocrystals from a carbon black template.
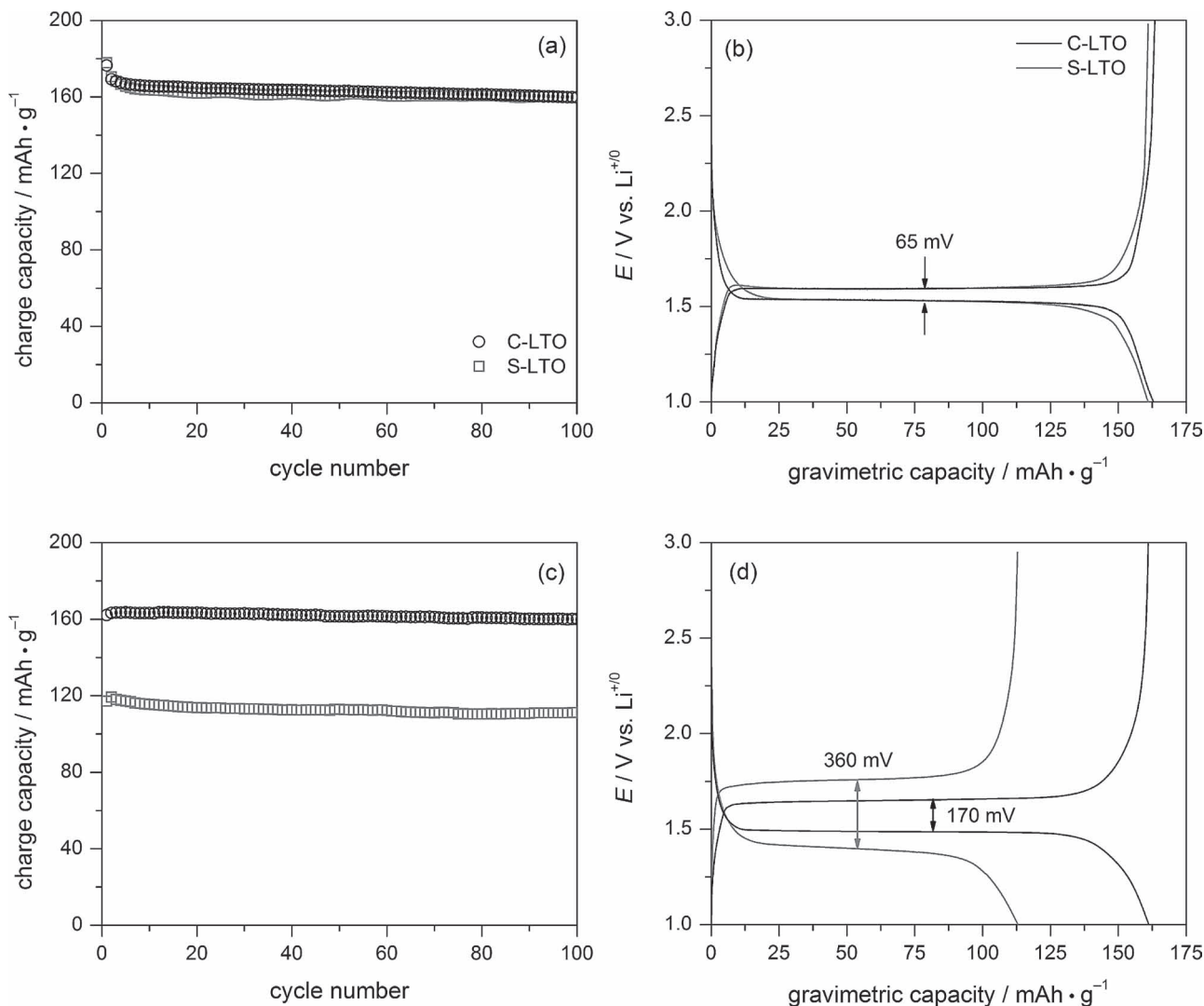
Figure 4. (a) Gravimetric charge capacity of C-LTO (black) and S-LTO (gray) cycled galvanostatically at 1 C; (b) individual charge and discharge curves for cycle 50 at 1 C; (c) galvanostatic cycling at 10 C; (d) charge discharge curves for cycle 50 at 10 C.

in Figure 4d. First, C-LTO shows a much larger capacity (161 mAh/g compared to 113 mAh/g for S-LTO). Second, C-LTO shows a smaller polarization–170 mV, which is *less than half* that observed for S-LTO, 360 mV. To demonstrate the repeatability of our cell fabrication, we assembled two additional cells; Figure S10 plots the charge capacity for three of each cell C-LTO and S-LTO cycled at both 1 C and 10 C current. All cells show virtually the same performance, and we conclude that isolated nanocrystals prepared by templated crystal growth not only retard the rate of deleterious side reactions that lead to capacity fade, but also result in a decrase in the charge-transfer resistance in the material.

To corroborate this result, we have measured the electro-chemical impedance of the thin-film electrodes and fit the data to include solution resistance, an *RC* circuit representing charge transfer, and a Warburg impedance representing ion diffusion. The resulting Nyqust plot and the equivalent circuit are shown together in **Figure 5**. R_{ct}, the charge-transfer resistance, is the diameter of the semicircle. **Table 1** shows the best

fit parameters for the EIS spectra. The chief result is that the cell composed of C-LTO has a signficantly smaller R_{ct}, 62.7 Ω vs. 197.8 Ω for S-LTO.

Although the fit to EIS data can give an estimate of the lithium-ion diffusion constant (D_{Li}), this method has the servere limation that it assumes the a perfectly homogeneous, planar electrode. Therefore, we turn to galvanostatic intermittent titration technique[33,34] (GITT) measurements to provide estimates of the lithium-ion diffusion coefficient for both LTO samples. In this experiment, a small current pulse (0.2 C = 35 μA/cm^2) is applied for 10 min and the cell is then allowed to rest at open circuit for 2 h. Both the initial non-equilibrium voltage and the final equilibrium open circuit voltages are recored. Then, we calculate the lithium diffusion coefficient according to:

$$D_{Li} = \frac{4}{\pi r} \left(\frac{m_B V_M}{M_B S} \right)^2 \left(\frac{\Delta E_s}{\Delta E_t} \right)^2 \quad (\tau << L^2/D_{Li}) \quad (1)$$
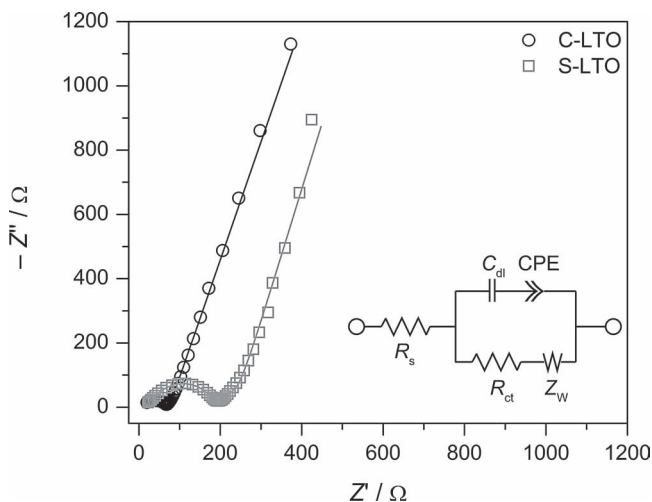
Figure 5. Nyquist plots for EIS data recorded for C-LTO (black) and S-LTO (gray). The inset shows the equivalent circuit used to obtain the fits (solid lines).

where D_{Li} is the lithium-ion diffusion coefficient; τ is the constant current pulse time; m_B is the active material mass on the electrode (1 mg); V_M is the molar volume of the compound (987 cm³/mol); M_B is the molar mass of the compound (459.09 g/mol); S is the electrode contact area with the electrolyte (85.4 cm² for C-LTO and 63.3 cm² for S-LTO, determined by BET surface-area measurements); ΔE_s is the difference between the steady potentials; and ΔE_t is the total transient voltage change of the cell for an applied galvanostatic current for the time τ. ΔE_s and the ΔE_t are determined in the experiment, and are marked in the **Figure 6**b as an example.

The GITT results and the calcuated diffusion constants for both C-LTO and S-LTO are ploted in Figure 6. The chemical formula of $Li_4Ti_5O_{12}$ can been re-written to represent the atomic positions in the standard spinel AB_2O_4 notation, $(Li)_{8a}[Li_{1/3},Ti_{5/3}]_{16d}(O_4)_{32e}$, where the subscripts outside of the parentheses represent the Wyckoff positions in the unit cell. This shorthand is simply 1/3 the stoichiometric formula, so in this notation, one mole of lithium inserts. Upon insertion, Li^+ residing on the 8a tetrahedral sites migrate to the previously vacant 16c octahedral sites (see Figure S7), and the product can be expressed as $[Li_2]_{16c}[Li_{1/3},Ti_{5/3}]_{16d}(O_4)_{32e}$.[35] In Figure 6, the curves are plotted showing one mole of lithium being added per mole of spinel on the x axis. The charging plateaus as determined by the open circuit potentials are greater than 1.55 V, showing that a 2 h rest period at open circuit is sufficient for the cell to reach equilibrium. The magnitude of D_{Li} ranges from 10^{-13} to 10^{-16} cm²·s⁻¹ throughout the insertion process,

regardless of the synthesis method employed. This behavior shows that lithium diffusion is not limited by particle aggregation in the S-LTO material. Also notable is that for both materials, the beginning and ending steps show diffusion that is ~10^3 faster than what is observed in the two-phase region.[36,37]

Despite the similarity in lithium-ion diffusion rates, the smaller charge-transfer resistance between nanocrystals and carbon black in C-LTO electrodes allows for better rate capability. To determine the rate capability of the C-LTO material, we cycled cells at 10 C, 20 C, 40 C, 80 C and 100 C current. The observed capacities and retention over the first 100 cycles are provided in **Figure 7**a. Capacity retention is excellent for all rates; even at 100 C current, 100% of the capacity at cycle 3 is retained after cycle 100. At this rate, the battery is capable of storing and releasing *all* of its charge in 36 s. In Figure 7b, the voltage profiles for the 50th cycle at each rate are plotted together.

Although the total energy stored in C-LTO and S-LTO is the same, 250 Wh/kg, for thin-film cells operated at low current (1 C), the energy density drops dramatically for S-LTO as the load increases. C-LTO stores 238 Wh/kg of energy even when cycled at 10 C, whereas the energy density of S-LTO decreases to 157 Wh/kg. Notably, C-LTO stores more energy (190 Wh/kg) at ten times the load (100 C current) compared to S-LTO at 10 C, shown in the Ragone plot of **Figure 8**. This result best highlights the electrochemical advantage of our carbon-templated nanocrystal growth.

We note that practical battery use in electric vehicles requires greater density of the active material on the working electrode. Therefore, we assembled three additional cells using C-LTO with an active material mass loading of 4 mg/cm², and cycled the cells at 1 C current. As observed in Figure S11, all three cells show similar capacity retention for the first 100 cycles compared to those cells with only 1 mg/cm² C-LTO cells. We note that the polarization gap is ever so slightly larger (72 mV vs. 65 mV). As a result, our work provides material that shows real promise in the search for safe, high power, high energy density lithium-ion battery anodes—ones competent enough to replace graphite.

3. Discussion

Although there are other examples of employing a template during the synthesis of LTO to reduce particle size, our work improves upon the use of a template to reduce particle size *without* subsequent aggregation of nanoparticles. The typical approach is to use a soft template and surfactant such as cetyltrimethylammonium bromide (CTAB)[38] or copoly-mers.[39,40] However, this strategy results in all of the nutrients residing
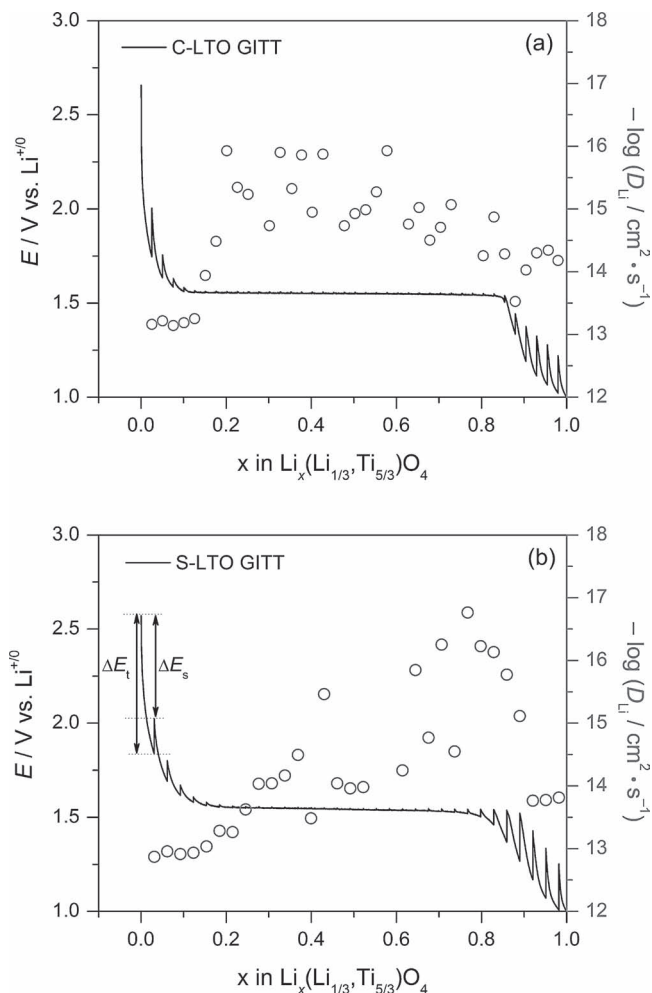
Table 1. EIS fit parameters for C-LTO and S-LTO.

Compound	R_s [Ω]	R_{ct} [Ω]	Z_W-R [Ω]	Z_W-T [s]	Z_W-P	C_{dl} [10^{-6} F]	CPE-T [10^{-4} s]	CPE-P
C-LTO	19.9	62.72	53.45	0.3375	0.4152	1.67	5.06	0.303
S-LTO	23.2	197.8	224.5	0.3194	0.401	2.31	3.62	0.364

R-resistance, T-time constant or capacitance, P-an exponent[48] $Z_{CPE} = 1/[T(i \cdot \omega)^P]$ $Z_W = R \cdot ctnh\,[(i \cdot T \cdot \omega)^P]/(i \cdot T \cdot \omega)^P$

ADVANCED
ENERGY
MATERIALS
www.advenergymat.de

Materials
Views
www.MaterialsViews.com

Figure 6. GITT curves for C-LTO, (a) and S-LTO (b). The gray circles in each plot represent the diffusion constant calculated from Equation 1, as described in the text.

Figure 7. (a) Rate capability of C-LTO cycled at varying current; (b) individual charge and discharge curves for the 50th cycle at each current. Note that polarization increases as C rate increases.

in a hydrophilic core. Then, nucleation and growth also occur within this small core and the particles aggregate as crystallite surfaces come into contact. Alternatively, the carbon template that we use keeps all of the nutrients contained without allowing as many of the growing nanocrystals on the surface to come into close contact. Burning off the template seeds nucleation, and growth is limited as the solvent is removed. This growth method gives well isolated C-LTO nanocrystals. The chemistry differences between these two approaches toward growing nanomaterials using a template are illustrated in **Scheme 1**. In our method, minimizing particle aggregation within nanoscale materials has important consequences in the energy density and power of the resulting thin-film electrodes, as we now explain.

First, we consider the three elementary steps in the charge and discharge of a titanium-based lithium-ion battery: 1) lithium-ion diffusion in bulk; 2) charge-transfer from the ion-conducting oxide to the electron-conducting carbon; and 3) ion diffusion in the electrolyte.[41] Not surprisingly, the lithium-ion diffusion constants of C-LTO nanocrystals and S-LTO aggregates
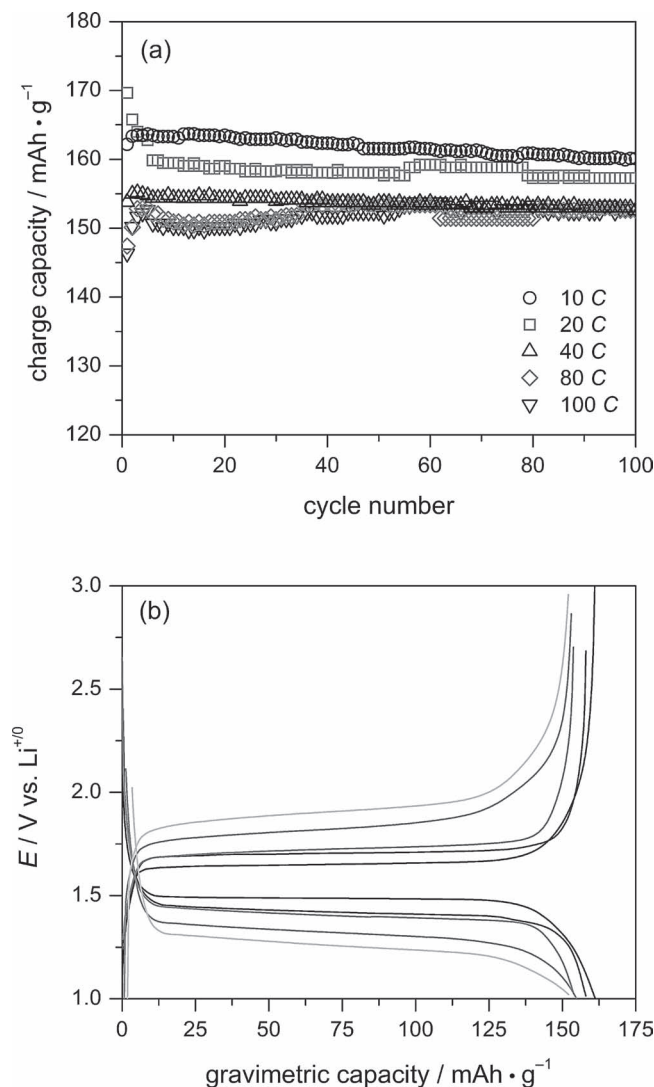
are the same, and match those reported for bulk samples. The key conclusion is that rate of lithium-ion diffusion in LTO is extremely slow regardless of morphology or use of a template to prepare nanoparticles. Therefore, in a Li-ion battery, LTO nanomaterials are vital because they shorten the lithium path.

Next, we note that since lithium-ion diffusion is slow, the observation of high rate capability requires that charge transfer between the oxide nanocrystals and the conductive carbon be extremely rapid. Indeed, C-LTO electrodes demonstrate R_{ct} that is 3 times smaller than that observed in S-LTO electrodes, and represents the hallmark of our work. We propose that the superior rate capability arises because there is less aggregation within nanocrystals grown using a carbon template. Therefore, there is greater surface contact between the nanocrystals and the conductive carbon added to the thin-film electrode slurry. In nanoparticle aggregates, charge transfer is limited because too many LTO crystallites adhere only to other non-conductive
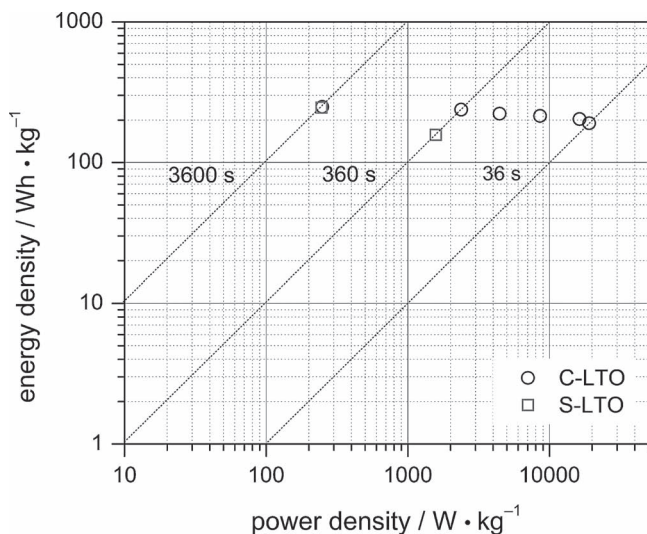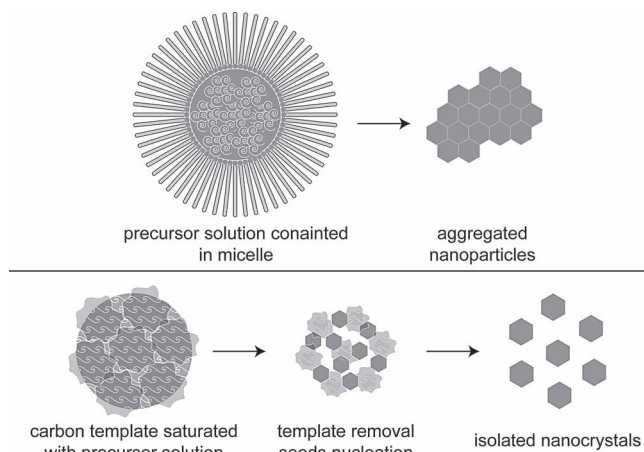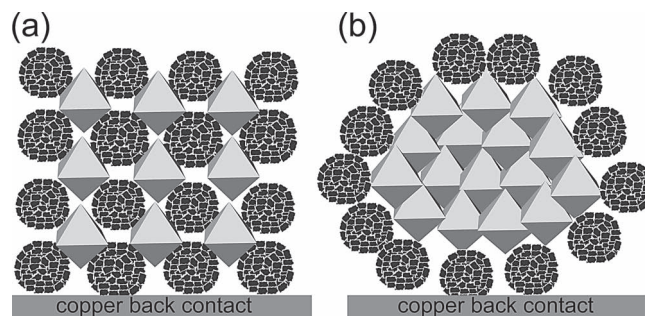
www.MaterialsViews.com

ADVANCED
ENERGY
MATERIALS
www.advenergymat.de

FULL PAPER

Figure 8. Ragone plot for C-LTO (black) and S-LTO (gray).

Scheme 2. Greater conducting carbon-LTO nanocrystal contact in C-LTO (a), compared to S-LTO aggregates (b).

LTO crystallites in a percolated network rather than contacting the conducting carbon black in the slurry. **Scheme 2** illustrates this proposition.

Then, it has been proposed in the literature that the presence of Ti^{3+} in the prepared compound enhances the surface conductivity, and therefore accelerates the rate of charge transfer.[42,43] We performed low-temperature EPR spectroscopy and XPS measurments on our C-LTO and S-LTO materials. The data are presented in Figure S12; no evidence of Ti^{3+} either in bulk or on the surface of our synthesized material is detected by these methods. In the XP spectrum, two different chemical environments are identified ($^2P_{3/2}$ peaks at 458.0 eV and 459.2 eV), both of which correspond to Ti^{4+}.[44,45] The observation of two environments is likely ascribed to surface-bound carbonate or hydroxide;[46,47] surface Ti^{3+} would show its $^2P_{3/2}$ peak at lower binding energy. Of course, Ti^{3+} is formally present as lithium inserts, with the average oxidation state of titanium in Li$_7$Ti$_5$O$_{12}$ being +3.4.

Finally, we bolster this hypothesis by examining the electrochemistry of other LTO samples in **Table 2**. We compare our LTO nanocrystals against bulk LTO, nanoparticle agglomerates of LTO prepared without templating, and aggregates prepared with CTAB templating. We note that the charge storage capacity of LTO is similar to what other researchers report. It should be; it is an inherent property of the material. At the reversible limit (i.e., cycled sufficiently slowly), all LTO materials would show a gravimetric capacity of 175 mAh/g. In functional materials, however, two new factors come into play. We have highlighted the first factor in the preceding paragraphs. The capacity is smaller because the end user has no time to wait for Li$^+$ to insert throughout the entire material to store charge. The second is that the sheer amount of charge stored in a material is irrelevant if that charge has little stored energy. The hysteresis losses in nanomaterials prepared by classic methods render high rate cycling impractical; with a voltage difference between charge and discharge of > 250 mV, over 30% of the energy is lost as heat (determined by integrating the difference in areas under the charge and discharge curves). Thin-film electrodes composed of our nanocrystals show marked improvement, with a capacity retention of 90% at 1 C current, and 100% at 100 C.

Scheme 1. Comparison between soft-templating methods (top) and carbon templating (bottom) for LTO crystal growth.

Table 2. Electrochemical Comparison of LTO Synthesized by Varying Methods.

Compound	Capacity [mAh•g^{-1}]	Polarization [mV]	Reference
CTAB-LTO[a]	~135 at 1000 mA/g	>250	[38]
3DOM-LTO[b]	~145 at 0.625 mA/g (~10 C)	N/A	[34]
Hollow sphere-LTO[c]	~100 at 10 C	>250	[49]
carbon coated LTO sphere[d]	~110 at 10 C	>250	[50,51]
S-LTO[e]	113 at 10 C	360	this work
C-LTO[f]	161 at 10 C	170	this work

[a]porous structrue with surface area 219.2 m^2/g; [b]macroporous structure; No conductive agent in electrode; [c]using micron sized carbon sphere as a hard template; [d]using pitch as a carbon coating agent (5.2 wt%); 70 µm[e]1 mg/cm^2 loading(30 µm); carbon black template employed; [f]1 mg/cm^2 loading(30 µm); direct solution method

FULL PAPER

4. Conclusion

We have pioneered a crystal growth process for oxide nanocrystals that relies on templating with amorphous carbon. The template serves two purposes—decreasing the particle size and preventing aggregative growth. As a result, thin-film electrodes comprising $Li_4Ti_5O_{12}$, a sought after material for lithium-ion battery anodes, show dramatically improved energy density retention when cycled at high current. We demonstrate that this improvement arises because charge transfer between isolated nanocrystals and the conducting carbon in the electrode is rapid, unlike to the larger charge-transfer resistance observed in a percolated network of nanoparticle aggregates.

5. Experimental Section

General Considerations: Lithium metal 99.9% (metal basis) was purchased from Alfa Aesar. Titanium isopropoxide 97% was purchased from Sigma Aldrich, and it was distilled prior to storing in a Vacuum Atmospheres OmniLab glove box under an argon atmosphere. Ethanol (200 proof) was purchased from Decon Labs. Toluene was purchased from EMD milipore and purified through a VAC solvent purifier unit. Acetylene black (carbon black,/CB) was purchased from Strem Chemicals. CB was kept in a Fisher Scientific™ oven at 150 °C prior to use. Deuterated toulene (99.5%) and ethanol (99.5%) were purchased from Cambridge Isotope Laboratories.

Powder X-ray diffraction patterns were collected on a Bruker D8 Advance diffractometer with a Lynx-Eye detector and parallel beam optics using Cu-Kα radiation ($\lambda = 1.54184$ Å). The patterns were indexed and refined using the Bruker TOPAS software. Scanning electron microscopy images were obtained on an FEI Nova Nanolab SEM/FIB at an accelerating voltage of 10 kV. High resolution transmission electron microscopy was performed on a JEOL 3011 TEM with a LaB$_6$ electron source operated at 300 kV. The samples were prepared by sonicating a dispersion of powdered sample in tetrahydrofuran and drop casting the resulting suspension onto a Cu grid with an ultra-thin holy carbon film (Ted Pella). The samples were heated to 60 °C in a Fisherbrand vacuum oven prior to the measurement. X-ray photoelectron spectra were collected with a Krato Axis Ultra spectrometer with a monochromatic Al Kα source and a charge neutralizer system was used for all the analyses. The data collected were fit using Casa™ XPS software package 2.3.15. Electron paramagnetic resonance spectra were recorded on a Bruker X-band (9.3 GHz) EMX spectrometer at 6 K. The microwave power and frequency were 20.51 mW and 9.28 GHz respectively, with a modulation amplitude of 1.00 G at 100 kHz. Thermal analyses were obtained with a TGA7 Thermogravimetric Analyzer (Perkin Elmer™) at a heating rate of 10 °C/min. under a flow of air. Raman spectra were obtained using a Renishaw Ramascope Raman Spectrometer. All spectra were taken under 785 nm laster excitation with 1.1 mW incident power. NMR spectra were recorded on a Varian MR400 400 MHz spectrometer using toluene-d_8 and ethanol-d_6 solvents.

Synthesis: Lithium metal (typically 27 mmol) was dissolved in 40 mL of ethanol in a Schlenk flask charged with nitrogen. Titanium isopropoxide was dissolved in 60 mL of dry toluene in an argon atmosphere glove box. These two reagents were mixed together by cannula transfer to give a transparent solution containing both lithium and titanium synthons (200 mL total, lithium to titanium molar ratio is 4:5 and the volumetric ratio of ethanol to toluene is adjusted to 2:3). This precursor solution is stable under ambient room atmosphere, as evidenced by an unchanged NMR spectrum.

To prepare the lithium titanate directly from this precursor solution (S-LTO), a 15 mL aliquot of the precursor stock solution was poured into a 23 mL scintillation vial and placed in the vacuum oven at 60 °C for 2 h in order to remove excess solvent. The resulting white residue was transferred to an alumina boat and annealed in an MTI muffle furnace

at 700 °C for 1 h with both heating and cooling rates of 10 °C/min. From this reaction, ~100 mg of product is isolated.

To prepare lithium titanate using a carbon black templating method (C-LTO), typically, 1 g of carbon black was added to 50 mL of the precursor solution. This mixture was stirred overnight and then sonocated for 2 h to form a well dispersed suspension. Then, the resulting thick slurry was centrifuged to give a residue coated with carbon black. This residue was dried in the vacuum oven at 60 °C for 2 h, then annealed at 700 °C for 1 h as described above. To study the growth mechanism of C-LTO nanocrystals, other annealing temperatures (400 °C and 450 °C) were employed, where carbon is not completely oxidized.

Electrochemical Measurements: Thin-film electrodes were prepared by mixing the synthesized material, carbon black and poly(vinylidene) difluoride (PVDF, purchased from Alfa Aesar) (mass ratio of 75:15:10) with a Thinky AR-100 rotation/revolution super mixer. *N*-methyl-2-pyrrolidone (NMP, 99+%, purchased from Alfa Aesar) was added to dissolve the PVDF completely and to maintain an appropriate viscosity of the resulting black slurry. This material was then coated onto a de-greased copper foil using the doctor blade method, and the foil was dried in the vacuum oven at 120 °C overnight prior to assembling the cell in order to minimize surface-bound water. The working electrode and glass fiber separator (GF/D) were cut and fit into a Swagelok™ PTFE union in the argon glove box. The active material loading is approximately 1 mg/cm^2 or 4 mg/cm^2. The electrode masses were measured using a Sartorius™ ME36S microbalance. In all cells, the electrolyte solution was composed of 1 M lithium hexafluorophosphate (99.99+%, Sigma Aldrich) dissolved in 2:1 (v/v) ethylene carbonate (99%, anhydrous, Sigma Aldrich) and diethyl carbonate (99+%, anhydrous, Sigma Aldrich), and lithium foil was used as both the auxiliary and reference electrode in a 2-electrode configuration.

Galvanostatic charge/discharge curves were recorded on a CH Instruments 660C electrochemical workstation with a voltage window of 1 to 3 V (*vs.* Li$^{+/0}$). The polarization gaps due to hysteresis in the charge and discharge profiles are reported at one half the gravimetric capacity values. Galvanometric intermittent titration technique (GITT) measurements were collected using a customized Vencon UBA5 battery analyzer. In GITT measurements, a galvanostatic pulse of 0.2 *C* was applied for 600 s followed by relaxation at open circuit 2 h. The cut-off voltage is set to 1 V. Prior to the GITT test, all cells were galvanostatically discharged to 3 V with a cut-off current limit of 10 nA followed by a 2 h rest period at open circuit. Electrochemical impedance spectra (EIS) were collected using an Autolab PGSTAT302N with a FRA (frequency reponse analysis) module. Batteries were cycled ten times between 1.0 and 3.0 V at 1 *C* current before the measurements. The cycling behavior was stopped at half the charging capacity on the last cycle, at which point all of the cells were stored in an argon glovebox overnight such that the spectra start at the open circuit potential, 1.55 V. The EIS were recorded in a frequency range from 10^5 to 10^{-2} Hz with AC perturbation was ±10 mV. Zview™ software package was used for the data fitting.

Supporting Information

Supporting Information is available from the Wiley Online Library or from the author. The Supporting information contains NMR spectrum of the precursor solution, X-ray diffraction patterns and Rietveld refinement, thermogravimetric analysis, IR-, EPR-, and XP spectra.

Acknowledgements

www.MaterialsViews.com

ADVANCED
ENERGY
MATERIALS
www.advenergymat.de

FULL PAPER

[1] G.-N. Zhu, Y.-G. Wang, Y.-Y. Xia, *Energy Environ. Sci.* **2012**, *5*, 6652.

[2] J. Jiang, J. R. Dahn, *J. Electrochem. Soc.* **2006**, *153*, A310.

[3] L.-F. Cui, R. Ruffo, C. K. Chan, H. Peng, Y. Cui, *Nano Lett.* **2009**, *9*, 491.

[4] J. Gu, S. M. Collins, A. I. Carim, X. Hao, B. M. Bartlett, S. Maldonado, *Nano Lett.* **2012**, *12*, 4617.

[5] K. M. Colbow, J. R. Dahn, R. R. Haering, *J. Power Sources* **1989**, *26*, 397.

[6] M. M. Thackeray, *J. Electrochem. Soc.* **1995**, *142*, 2558.

[7] F. Ronci, P. Peale, B. Scrosati, S. Panero, V. Rossi Albertini, P. Perfetti, M.di Michiel, J. M. Merino, *J. Phys, Chem. B* **2002**, *106*, 3082.

[8] L. Kavan, J. Rathousky, M. Grätzel, V. Shklover, A. Zukal, *J. Phys. Chem. B.* **2000**, *104*, 12012.

[9] C. H. Chen, J. T. Vaughey, A. N. Jansen, D. W. Dees, A. J. Kahaian, T. Goacher, M. M. Thackeray, *J. Electrochem. Soc.* **2001**, *148*, A102.

[10] L. Kavan, J. Procházka, T. M. Spitler, M. Kalbáč, M. Zukalová, T. Drezen, M. Grätzel, *J. Electrochem. Soc.* **2003**, *150*, A1000.

[11] J. Li, Z. Tang, Z. Zhang, *Electrochem. Commun.* **2005**, *7*, 894.

[12] A. S. Aricò, P. Bruce, B. Scrosati, J.-M. Tarascon, W. van Schalkwijk, *Nature Mater.* **2005**, *4*, 366–377.

[13] K. Naoi, W. Naoi, S. Aoyagi, J. Miyamoto, T. Kamino, *Acc. Chem. Res.* **2012**, DOI: 10.1021/ar200308.

[14] K. Naoi, S. Ishimoto, Y. Isobe, S. Aoyagi, *J. Power Sources* **2010**, *195*, 6250.

[15] Y. Tang, F. Huang, W. Zhao, Z. Liu, D. Wan, *J. Mater. Chem.* **2012**, *22*, 11257.

[16] B. Zhang, Y. Liu, Z. Huang, S. Oh, Y. Yu, Y.-W. Mai, J.-K. Kim, *J. Mater. Chem.* **2012**, *22*, 12133.

[17] H.-K. Kim, S.-M. Bak, K.-B. Kim, *Electrochem. Commun.* **2010**, *12*, 1768.

[18] Y.-Q. Wang, L. Gu, Y.-G. Guo, H. Li, X.-Q. He, S. Tsukimoto, Y. Ikuhara, L.-J. Wan, *J. Am. Chem. Soc.* **2012**, *134*, 7874.

[19] Y. F. Tang, L. Yang, Z. Qiu, J. S. Huang, *Electrochem. Commun.* **2008**, *10*, 1513.

[20] J. Kim, J. Cho, *Solid-State Lett.* **2007**, *10*, A81.

[21] S.-L. Chou, J.-Z. Wang, H.-K. Liu, S.-X. Dou, *J. Phys. Chem. C.* **2011**, *115*, 16220.

[22] D. H. Kim, Y. S. Ahn, J. Kim, *Electrochem. Commun.* **2005**, *7*, 1340.

[23] Y. Hao, Q. Lai, Z. Xu, X. Liu, X. Ji, *Solid State Ionics* **2005**, *176*, 1201.

[24] Y. H. Rho, K. Kanamura, *J. Solid State Chem.* **2004**, *177*, 2094.

[25] K. Kanamura, N. Akutagawa, K. Dokko, *J. Power Sources* **2005**, *146*, 86.

[26] J. M. Feckl, K. Fominykh, M. Döblinger, D. F.-Rohlfing, T. Bein, *Angew. Chem. Int. Ed.* **2012**, *51*, 7459.

[27] C. M. Julien, M. Massot, K. Zaghib, *J. Power Sources* **2004**, *136*, 72.

[28] M. M. Thackeray, *J. Am. Ceram. Soc.* **1999**, *82*, 3347.

[29] P. Scherrer, *Göttinger Nachrichten Gesell.* **1918**, *2*, 98.

[30] X. Hao, M. H. Austin, B. M. Bartlett, *Dalton Trans.* **2012**, *41*, 8067.

[31] K. Zaghib, M. Simoneau, M. Armand, M. Gauthier, *J. Power Sources* **1999**, *81-82*, 300.

[32] L. Kavan, M. Grätzel, *Electrochem. Solid-State Lett.* **2002**, *5*, A39.

[33] M. Wagemaker, D. R. Simon, E. M. Kelder, J. Schoonman, C. Ringpfeil, U. Haake, D. Lützenkirchen-Hecht, R. Frahm, F. M. Mulder, *Adv. Mater.* **2006**, *18*, 3169.

[34] W. Weppner, R. Huggins, *J. Electrochem. Soc.* **1977**, *124*, 1569.

[35] J. R. Macdonald, L. D. Potter Jr. *Solid State Ionics* **1987**, *23*, 61.

[36] E. M. Sorensen, S. J. Barry, H.-K. Jung, J. R. Rondinelli, J. T. Vaughey, K. R. Poeppelmeier, *Chem. Mater.* **2006**, *18*, 482.

[37] M. Wilkening, R. Amade, W. Iwaniak, P. Heitjans, *Phys. Chem. Chem. Phys.* **2007**, *9*, 1239.

[38] M. Wagemaker, E. R. H. van Eck, A. P. M. Kentgens, F. M. Mulder, *J. Phys. Chem. B.* **2009**, *113*, 224.

[39] J. Chen, L. Yang, S. Fang, S. I. Hirano, K. Tachibana, *J. Power Sources* **2012**, *200*, 59.

[40] J. Huang, Z. Jiang, *Solid-State Lett.* **2008**, *11*, A116.

[41] B. Smarsly, D. Grosso, T. Brezesinski, N. Pinna, C. Boissière, M. Antonietti, C. Sanchez, *Chem. Mater.* **2004**, *16*, 2948.

[42] L. Cheng, X. L. Li, Liu, J. H. H. M. Xiong, P. W. Zhang, Y. Y. Xia, **2007**, *154*, A692.

[43] X. Chen, X. Guan, L. Li, G. Li, *J. Power Sources* **2012**, *210*, 297.

[44] Y. Wang, H. Liu, K. Wang, H. Eiji, Y. Wang, H. Zhou, *J. Mater. Chem.* **2009**, *19*, 6789.

[45] D. Gonbeau, C. Guimon, G. Pfister-Guillouzo, *Surf. Sci.* **1991**, *254*, 81.

[46] R. P. Vasquez, *J. Electron Spectrosc. Relat. Phemon.* **1991**, *56*, 217.

[47] M. Q. Snyder, W. J. DeSisto, C. P. Tripp, *App. Surf. Sci.* **2007**, *253*, 9336.

[48] B. A. Boukamp, *Solid State Ionics.* **1986**, *20*, 31.

[49] N. He, B. Wang, J. Huang, *J. Solid State Electrochem.* **2010**, *14*, 1241.

[50] H.-G. Jung, M. W. Jang, J. Hassoun, Y.-K. Sun, B. Scrosati, *Nat. Commun.* **2011**, *2*, 1.

[51] H.-G. Jung, S.-T. Myung, C. S. Yoon, S.-B. Son, K. H. Oh, K. Amine, B. Scrosati, Y.-K. Sun, *Energy Environ. Sci.* **2011**, *4*, 1345.